



HAL
open science

Impact of seismicity on Nice slope stability-Ligurian Basin, SE France: a geotechnical revisit

Alexander Roesner, Gauvain Wiemer, Stefan Kreiter, Stefan Wenau, Ting-Wei Wu, Françoise Courboux, Volkhard Spiess, Achim Kopf

► **To cite this version:**

Alexander Roesner, Gauvain Wiemer, Stefan Kreiter, Stefan Wenau, Ting-Wei Wu, et al.. Impact of seismicity on Nice slope stability-Ligurian Basin, SE France: a geotechnical revisit. *Landslides*, 2019, 16 (1), pp.23-35. 10.1007/s10346-018-1060-7 . hal-02238556

HAL Id: hal-02238556

<https://hal.science/hal-02238556>

Submitted on 27 Nov 2020

HAL is a multi-disciplinary open access archive for the deposit and dissemination of scientific research documents, whether they are published or not. The documents may come from teaching and research institutions in France or abroad, or from public or private research centers.

L'archive ouverte pluridisciplinaire **HAL**, est destinée au dépôt et à la diffusion de documents scientifiques de niveau recherche, publiés ou non, émanant des établissements d'enseignement et de recherche français ou étrangers, des laboratoires publics ou privés.

Landslides

DOI 10.1007/s10346-018-1060-7

Received: 7 March 2018

Accepted: 5 September 2018

© Springer-Verlag GmbH Germany

part of Springer Nature 2018

A. Roesner · G. Wiemer · S. Kreiter · S. Wenau · T.-W. Wu · F. Courboux · V. Spiess · A. Kopf

Impact of seismicity on Nice slope stability—Ligurian Basin, SE France: a geotechnical revisit

Abstract The shallow Nice submarine slope is notorious for the 1979 tsunamigenic landslide that caused eight casualties and severe infrastructural damage. Many previous studies have tackled the question whether earthquake shaking would lead to slope failure and a repetition of the deadly scenario in the region. The answers are controversial. In this study, we assess for the first time the factor of safety using peak ground accelerations (PGAs) from synthetic accelerograms from a simulated offshore Mw 6.3 earthquake at a distance of 25km from the slope. Based on cone penetration tests (CPTu) and multichannel seismic reflection data, a coarser grained sediment layer was identified. In an innovative geotechnical approach based on uniform cyclic and arbitrary triaxial loading tests, we show that the sandy silt on the Nice submarine slope will fail under certain ground motion conditions. The uniform cyclic triaxial tests indicate that liquefaction failure is likely to occur in Nice slope sediments in the case of a Mw 6.3 earthquake 25km away. A potential future submarine landslide could have a slide volume ($7.7 \times 10^6 \text{m}^3$) similar to the 1979 event. Arbitrary loading tests reveal post-loading pore water pressure rise, which might explain post-earthquake slope failures observed in the field. This study shows that some of the earlier studies offshore Nice may have overestimated the slope stability because they underestimated potential PGAs on the shallow marine slope deposits.

Keywords Submarine landslides · Liquefaction · Earthquakes · Post-earthquake slope failure · Arbitrary triaxial loading · Nice

Introduction

The 1979 Airport Landslide offshore Nice is a well-examined submarine landslide example (Anthony and Julian 1997; Dan et al. 2007; Gennesseaux et al. 1980; Sultan et al. 2004). The catastrophic failure on the Nice shallow submarine slope triggered a tsunami wave, which hit the coastline along the Ligurian Sea causing eight casualties and infrastructural damage (Dan et al. 2007; Migeon et al. 2006; Sahal and Lemahieu 2011). The interplay of land reclamation operations 6 months before the failure, extra loading by embankments of the extended Nice airport and heavy rainfall of 250 mm for 4 days before the failure most likely created an unstable artificial delta front slope, which collapsed on the 16 October 1979 (Anthony 2007; Anthony and Julian 1997; Dan et al. 2007; Kopf et al. 2016). Seismic loading did not trigger the 1979 failure; nevertheless, seismic loading is a prominent trigger for submarine landslides (Haque et al. 2016; Leynaud et al. 2017; Sultan et al. 2004), and the junction between the southern French-Italian Alps and the Ligurian Basin near Nice faces the highest seismicity in western Europe (Larroque et al. 2009; Salichon et al. 2010). Therefore, earthquake shaking needs to be considered as a potential trigger for future slope failures offshore Nice.

Granular loose sediments tend to contract under the cyclic loading imposed by earthquake shaking, which can transfer normal stress from the granular matrix onto the pore water if the soil is saturated and largely unable to drain during shaking. This eventually leads to zero normal effective stress and the sediment behaves as a liquid suspension; this process is called liquefaction (Idriss and Boulanger 2008; Ishihara 1985; Kramer 1996). The liquefaction potential is higher for loose than for dense granular sediments (Kramer 1996). In this context, the Nice slope sediment liquefaction potential is of special interest, because earthquake shaking may induce weakness in granular sediment layers and allow for the development of a shear plane of a submarine landslide (Sultan et al. 2004). In historical times, four devastating earthquakes, with intensities from 8 to 10 on the Mercalli scale and six more recent earthquakes since 1963, with magnitudes from 4 to 6, affected the Ligurian Basin (Migeon et al. 2006). Three historical tsunamis were generated by these earthquakes, damaging Ligurian Sea coastal infrastructure and causing casualties (Courboux et al. 2007; Ferrari 1991; Migeon et al. 2006). With approximately 2 million inhabitants and more than 5 million tourists every year, these events highlight the vulnerability of the densely populated Nice coastline, if a future tsunami were to strike the area.

Over the last two decades, several studies characterized the Nice submarine slope sediments and their stability via in situ measurements (Stegmann et al. 2011; Steiner et al. 2015; Sultan et al. 2010), laboratory experiments (Kopf et al. 2016; Stegmann and Kopf 2014; Sultan et al. 2004), high-resolution bathymetric data analysis (Kelner et al. 2016; Migeon et al. 2012), Envisat InSAR data (Cavalié et al. 2015), and numerical modeling (Dan et al. 2007; Steiner et al. 2015). These studies present contradictory results and interpretations concerning the Nice slope stability under earthquake ground motions. Sultan et al. (2004) compared cyclic triaxial tests to cyclic loads that may occur during earthquakes on the Nice slope with varying peak ground accelerations (PGAs) of 0.5, 1.0, and 1.5 m s^{-2} . They found that the cyclic loading caused by these PGAs were too low to initiate liquefaction failure in the tested sediment. They concluded that the liquefaction failure potential of Nice slope sediments is low due to a lack of loose sediment. In contrast, Dan et al. (2007) discussed that cyclic shaking may induce liquefaction in sand and silt interbeds present on the Nice slope. Ai et al. (2014) studied the cyclic stresses required for failure of the deeper continental slope offshore Nice and concluded that earthquakes with M 6.1–6.5 in an epicentral distance of <15 km from the Nice slope are sufficient to initiate slope failure. The latest study in the Nice shallow submarine slope area by Kopf et al. (2016), however, stated that seismic loading is unlikely to be sufficient to trigger a major landslide unless an earthquake with a magnitude larger than the magnitudes of known historical events occurs.

113 Salichon et al. (2010) simulated realistic ground motions generated by a potential future Mw 6.3 earthquake that occurs on a reverse fault 25 km offshore Nice. They provided evidence for the occurrence of PGAs larger than any other geotechnical study in this region ever considered. The simulated accelerograms show median PGA values of up to 5.8 m s^{-2} . These values exceed those considered in the slope stability analysis by Sultan et al. (2004) by a factor of approximately four.

121 Based on these facts, we revisit the Nice shallow submarine slope area and investigate the seismic slope stability with cyclic triaxial tests with loading patterns and amplitudes based on the simulated accelerograms by Salichon et al. (2010). For this purpose, we used classic uniform cyclic triaxial and new arbitrary triaxial tests and compare them. The confining stress in the triaxial tests is based on cone penetration tests (CPTu) and seismic data interpretation.

129 **Background**

130 **Geological setting**

131 The Ligurian Basin was formed via rifting and seafloor spreading in the late Oligocene (Rehault et al. 1984; Savoye et al. 1993; Savoye and Piper 1991). It is a back-arc basin originating from the roll back of the Apennines-Maghrebides subduction zone. The offshore structure in the Ligurian Basin consists of a northern extensional margin with an east-northeast (ENE) trending graben, which is mainly related to southeast dipping faults. Nowadays,

138 the convergence rate between Africa and Eurasia is $4\text{--}5 \text{ mm a}^{-1}$ in $N 309 \pm 5^\circ$ direction (Nocquet 2012).

139
140 The Nice continental margin morphology is dominated by the Var river, a 135 km long river draining a 2820-km^2 area from the Alps towards the city of Nice (Fig. 1). The Var river transports 10 million $\text{m}^3 \text{ a}^{-1}$ of fine suspended sediments as well as 0.1 million $\text{m}^3 \text{ a}^{-1}$ of gravel (Dubar and Anthony 1995; Mulder et al. 1998). Most of the sediment is transported downslope into the submarine Var canyon. The coastline has a narrow continental shelf with a width of a hundred meters up to 2 km and a steep submarine slope with an average slope angle of 13° (Cochonat et al. 1993). The sediment builds a Gilbert-type fan delta at the river mouth (Dubar and Anthony 1995). Dubar and Anthony (1995) described the three upper major sedimentary delta facies with a thickness of approximately 120 m from bottom to top: (1) clast-supported gravel with a matrix of sand, (2) fine-grained shallow marine and estuarine/paludal deltaic sediments, and (3) fine-grained floodplain and paludal sediments with gravel channel deposits. Kopf et al. (2016) presented a more detailed facies analysis based on 72 cores where they described silt/sand interbeds as one out of three Pliocene-Holocene sediment facies. The silt/sand interbeds are of high interest for seismic slope stability because cohesionless sediment layers have a high liquefaction potential under cyclic loading (Boulanger and Idriss 2006; Idriss and Boulanger 2008; Kramer 1996). Based on eight CPTu (Fig. 1a), Sultan et al. (2010) showed that these coarse-grained layers are present at different depths, down to ~ 30 mbsf at the Nice slope.

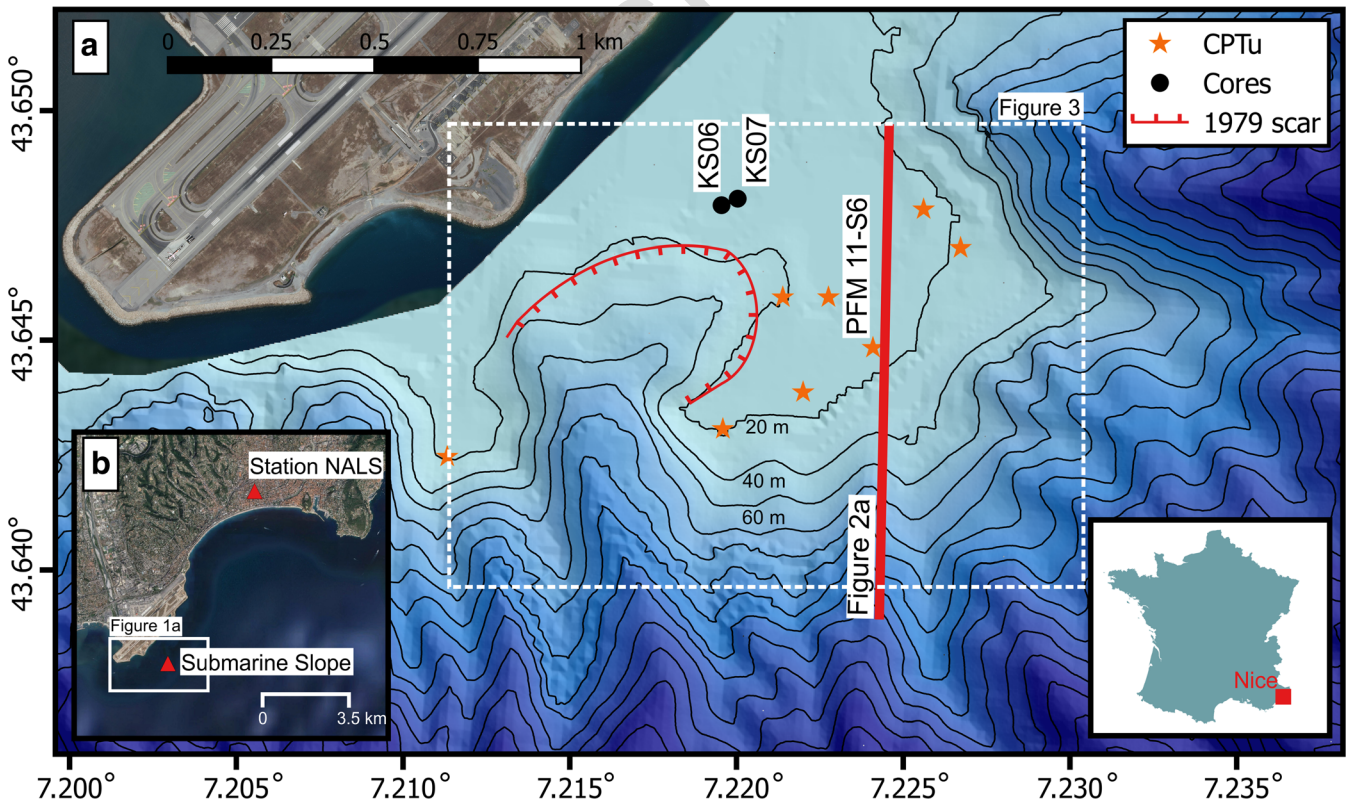


Fig. 1 a Map of the study area including the locations of Kullenberg cores KS06/07 and CPTu test. The red line indicates the seismic profile GeoB16-365 shown in Fig. 2a. The dashed box indicates the area presented in Fig. 3. b The inset shows the wider study area with the location of seismic station NALS. CPTu data and bathymetry were originally published by Sultan et al. (2010) and Dan et al. (2007)

165 **Simulated ground motions**

166 Ground motion simulations are often used to estimate accelera- 222
 167 tions of large earthquakes in regions with low seismicity, short 223
 168 recording history or when site effects are important. Salichon et al. 224
 169 (2010) used an empirical Green's function method developed by 225
 170 Kohrs-Sansorny et al. (2005) and widely applied since by several 226
 171 authors (Honoré et al. 2011; Wang et al. 2017). They simulated the 227
 172 ground motions that would be generated in the city of Nice by a
 173 Mw 6.3 earthquake occurring on a reverse fault 25 km offshore. 228
 174 This fault caused a Mw 4.5 earthquake in 2001 that was very well 229
 175 recorded by the permanent seismological network in the city of 230
 176 Nice (Courboux et al. 2007). The fault is part of a fault network 231
 177 that extends from the Gulf of Genoa in Italy to Nice (Larroque 232
 178 et al. 2011). The eastern part of this fault has been identified as 233
 179 the nucleation of the large M ~ 6.5–6.8 earthquake that killed 600 234
 180 people on the Ligurian coast in 1887 (Larroque et al. 2012). 235
 181 Salichon et al. (2010) used the recordings of the Mw 4.5 event in 236
 182 2001 on eight stations as empirical Green's function in order to 237
 183 reproduce the site effects in the city of Nice. Indeed, significant site 238
 184 effects have been detected in some areas with amplification factors 239
 185 of up to 20 at frequencies of 1–2 Hz (Semblat et al. 2000). The 240
 186 approach uses three steps: (1) selection of the actual recordings of 241
 187 a smaller earthquake used as an empirical Green's function (here 242
 188 the Mw 4.5 event that occurred on February 25th 2001), (2) genera- 243
 189 tion of a large number of source time functions that account for 244
 190 the possible variability of the rupture process of the modeled 245
 191 earthquake, and (3) convolution of both for each station. This 246
 192 approach created 500 simulated accelerograms for each station 247
 193 component. The NALS station (Fig. 1b) is of particular interest
 194 for our study because it is located on a 70-m-thick alluvial sedi-
 195 ment deposit that is regarded as similar to the site conditions at
 196 the shallow submarine Nice slope. The median PGAs simulated for
 197 a Mw 6.3 earthquake are 5.8 m s⁻² and 5.2 m s⁻² for the NS and EW
 198 component, respectively. More details on the simulation of ground
 199 motion and related PGAs for the city of Nice are given in Salichon
 200 et al. (2010). Five modeled accelerograms out of the 500 at station
 201 NALS by Salichon et al. (2010) are of special interest for our study.
 202 These accelerograms represent the possible range of ground moti-
 203 on and are categorized according to their PGAs in minimum,
 204 16th percentile, median, 84th percentile, and maximum (see also
 205 Table 2 in the appendix).

206 **Material and methods**

207 **Sample material**

208 In order to assess the shallow seismic slope stability offshore Nice,
 209 we performed earthquake simulating cyclic triaxial experiments
 210 on samples cored during the STEP 5 cruise in 2015 on the Nice
 211 shallow submarine slope (Thomas and Apprioual 2015). We took
 212 two Kullenberg cores KSo6 and KSo7, with respective lengths of
 213 3.81 m and 4.25 m adjacent to the 1979 slide scar (Fig. 1a). The
 214 cored sediment consists of silty sediment layers interbedded with
 215 predominantly clayey sediment similar to the sediment described
 216 by Kopf et al. (2016). Hereafter, the cored silty sediment layers are
 217 named sandy silt (Shepard 1954) or coarse-grained throughout the
 218 manuscript to emphasize that these layers constitute cohesionless
 219 and the coarsest sediment, thereby most prone to liquefaction,
 220 layers. These granular sediment layers are approximately 3–20 cm
 221 thick and are of special interest for the liquefaction analysis. Since

no silt or sand interbeds from 10 to 25 mbsf are available, we chose
 to use previously described coarse-grained interbeds from < 5 mbsf
 and consolidated them to confining stresses reigning at ~ 23 mbsf.
 This depth corresponds to the average depth of a prominent
 seismic reflector that correlates to CPTu profiles indicating
 coarse-grained sediments (Fig. 2).

228 **Geotechnical testing**

229 The sample material was geotechnically characterized by the grain
 230 size distributions, the Atterberg limits, and the parameters of the
 231 Mohr-Coulomb failure criterion. Grain size distributions of the
 232 coarse-grained sediments were measured via laser diffraction anal-
 233 ysis with a Coulter LS-13320 (see Agrawal et al. 1991; Loizeau et al.
 1994). We determined the Atterberg limits using the fall cone
 234 method (BS 1377-2:1990 1990; Kodikara et al. 2006) and the
 235 Mohr-Coulomb parameters using direct shear tests. The drained
 236 direct shear test samples were 56 mm in diameter and ~ 25 mm in
 237 height. The direct shear tests were performed in accordance with
 238 the German Institute for Standardization (DIN 18137-3 2002). The
 239 applied effective normal stress σ'_n ranged from 100 to 700 kPa and
 240 the shear displacement for each experiment was at least 12 mm.
 241 Effective normal stress, shear stress, as well as vertical and hori-
 242 zontal displacement were recorded at a frequency of 0.1 Hz. Shear
 243 rates were set to 0.02 mm min⁻¹ which is considered sufficiently
 244 slow to allow constant drainage and complete pore water pressure
 245 dissipation (DIN 18137-3 2002). The Mohr-Coulomb failure crite-
 246 rion is defined as:

$$\tau = c' + \sigma'_n \tan \phi' \quad (1)$$

248 where c' is the effective cohesion, i.e., the extrapolated intercept
 249 of the Mohr-Coulomb envelope with the y -axis, ϕ' the effective
 250 angle of internal friction and τ the shear strength. 252

253 **Liquefaction evaluation based on cyclic Triaxial testing**

254 Geotechnical liquefaction evaluation compares the seismic de-
 255 mand of expected earthquakes to the sediment cyclic resistance
 256 from laboratory experiments. Undrained cyclic shear tests deter-
 257 mine the sediment response to earthquake shaking under defined
 258 stress boundary conditions, with pore water pressure evolution
 259 and sediment deformation as primary output information. Ele-
 260 ment tests are conducted under undrained conditions to simulate
 261 essentially undrained field conditions during earthquake loading.
 262 These tests are the standard procedure for liquefaction assess-
 263 ment, since they test the material behavior under a defined uni-
 264 form stress state. The drainage state of a sediment in nature
 265 depends on the duration of the cyclic loading, the volume of the
 266 vulnerable sediment, its permeability, and the permeability of the
 267 surrounding sediment. The loading during an earthquake is fast,
 268 the tested sandy silt is not very permeable, and the surrounding
 269 finer grained sediments are even less permeable, that is why the in
 270 situ behavior is considered undrained even if the layer is not very
 271 thick. Earthquake shaking of Nice coarse-grained sediments was
 272 simulated via undrained cyclic shear strength experiments using
 273 the dynamic triaxial testing device (DTTD) (Wiemer and Kopf
 2017). The DTTD allows a wide range of testing configuration with
 274 its pressure compensated internal force sensor; further, details can
 275 be found in Kreiter et al. (2010). In this study, we applied the
 276 simplified procedure after Seed and Idriss (1971) and a new
 277

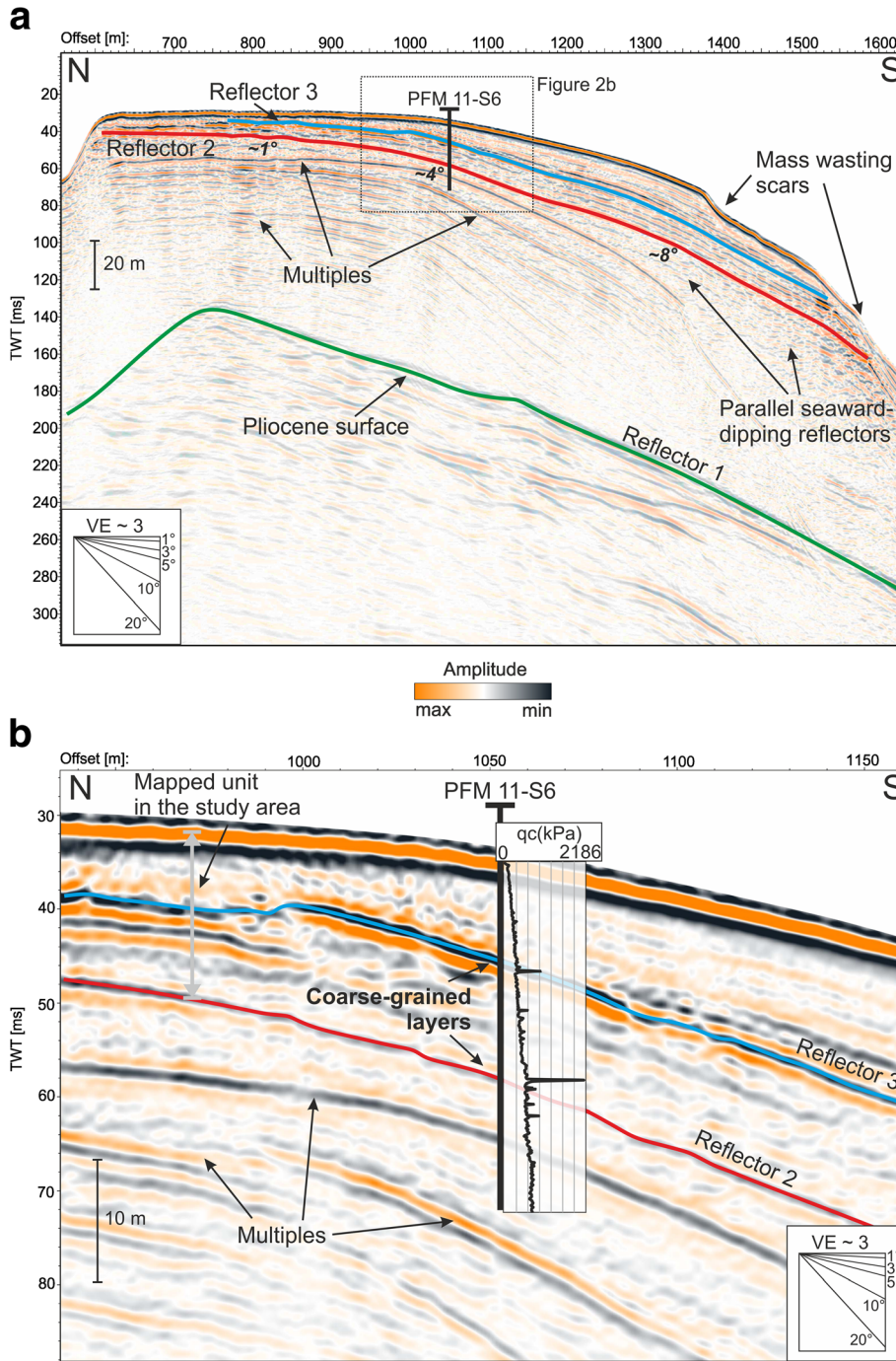


Fig. 2 a Multichannel seismic line GeoB16-365 shows the sedimentary succession of the Nice shelf. b Zoom in on seismic line GeoB16-365 with a scaled projection of CPTu measurement PFM 11-S6. The mapped reflectors R2 and R3 correspond to cone resistance maxima, suggesting coarse-grained sediment. CPTu data were originally published by Sultan et al. (2010)

278 arbitrary loading procedure to evaluate the liquefaction potential.
 279 The simplified procedure parameterizes an arbitrary earthquake-
 280 loading signal (accelerogram) to an equivalent uniform series of
 281 shear stress cycles. The amplitude of the uniform shear stress
 282 cycles is set to 65% peak amplitude of the arbitrary earthquake-

loading signal. The maximum cyclic shear stress at depth induced
 by an earthquake is estimated by:

$$\tau_{eq} = 0.65 \times \frac{a_{max}}{g} \times \sigma_{v,c} \times r_d \quad (2)$$

where a_{max} is the horizontal peak ground acceleration at ground surface, g is the acceleration of gravity, $\sigma_{v,c}$ is the total vertical stress at depth z (target depth = ~ 23 mbsf), and r_d is the stress reduction factor. The stress reduction factor accounts for the damping of the soil as an elastic body (Seed and Idriss 1971). Details regarding the input parameters and the stress reduction factor are given in the appendix. Here, we apply this method to five simulated accelerograms for the Mw 6.3 earthquake described by Salichon et al. (2010) representing the full range of ground motions at station NALS. The stress of the seismic demand on a soil layer is often expressed as the cyclic shear stress ratio:

$$CSR_{eq} = \frac{\tau_{eq}}{\sigma'_{v,c}} \quad (3)$$

where τ_{eq} is normalized by the total vertical effective stress $\sigma'_{v,c}$ at depth z .

Amplitude and equivalent number of uniform loading cycles constitute the cyclic demand of an earthquake to the sediment at depth. Liu et al. (2001) developed an empirical regression function that evaluates the number of equivalent uniform stress cycles as a function of magnitude, site conditions, i.e., soil site or rock site, and the site-source distance. From our Mw 6.3 earthquake striking a soil site from a distance of 25 km, we derive 12 equivalent uniform stress cycles.

Eight undrained cyclic triaxial experiments were performed on (i) coarse-grained reconstituted and (ii) coarse-grained carefully handled natural, undisturbed core samples from the cores KSo6 and KSo7. These tests split up in six uniform cyclic triaxial tests and two arbitrary triaxial tests (Table 1). We accomplished the uniform cyclic triaxial tests on five reconstituted samples and one core sample. The uniform test on the core sample was performed in order to investigate the influence of the structural effect on the cyclic shear strength. All samples had a diameter of 3.5 cm and a height of approximately 7.4 cm. The samples were isotropically consolidated to a mean consolidation stress of 570 kPa including 400 kPa back-pressure sufficient to reach full sample saturation. Consequently, the mean effective consolidation

stress p'_c is 170 kPa. Further details regarding sample preparation and consolidation can be found in the appendix. Uniform cyclic loading was applied at a frequency of 1 Hz. The cyclic loading is expressed with the triaxial cyclic shear stress ratio:

$$CSR_{cyc} = \frac{q_{cyc}}{2 \times \sigma'_{3c}} \quad (4)$$

$$q_{cyc} = \sigma'_1 - \sigma'_{3c} \quad (5)$$

where the single amplitude cyclic deviator stress q_{cyc} is calculated from the major principal effective stress σ'_1 and the minor principal effective consolidation stress σ'_{3c} . The CSR_{cyc} required for liquefaction in a specific number of loading cycles is also called soil cyclic resistance ratio (CRR). The excess pore water pressure Δu is expressed as excess pore pressure ratio:

$$r_u = \frac{\Delta u}{\sigma'_{3c}} \quad (6)$$

The number of cycles at failure were determined with the onset of liquefaction with $r_u = 1$.

The ratio of CRR and CSR_{eq} defines the factor of safety FS against liquefaction:

$$FS = \frac{CRR}{CSR_{eq}} \quad (7)$$

$FS > 1$ indicates a stable slope, whereas $FS < 1$ indicates slope failure.

The DTTD is well suited to load a sample with an arbitrary loading function (Kreiter et al. 2010). Hence, we skip all simplifications and load the sediment with a shear stress time series converted from a simulated accelerogram. We used a modified

t1.1 **Table 1** Triaxial test summary. The ID U1–6 are uniform cyclic and ID A1–2 arbitrary triaxial test. The abbreviation rec. stands for reconstituted sample

ID	Sample	Type	Water content	p'_c [kPa]	$CSR_{cyc}^a = CRR$	$CRR_{0.9}^b$	Void ratio	# of failure cycles
U1	KSo7_337cm	rec.	0.21	170	0.154	0.139	0.67	918
U2	KSo7_337cm	rec.	0.24	170	0.180	0.162	0.79	27
U3	KSo7_337cm	rec.	0.21	170	0.205	0.185	0.71	9
U4	KSo7_337cm	rec.	0.23	170	0.233	0.210	0.74	8
U5	KSo7_337cm	rec.	0.23	170	0.256	0.230	0.71	5
U6	KSo6_348cm	core	0.29	170	0.253	0.228	0.96	5
A1	KSo7_337cm	core	0.33	170	minimum modeled PGA	minimum modeled PGA	1.02	stable
A2	KSo7_337cm	core	0.29	170	16th percentile PGA	16th percentile PGA	0.96	failed

^a At failure

^b 90% of CRR, correction for unidirectional loading (appendix eq. (12))

353 version of eq. (2) to convert the provided minimum and 16th
 354 percentile accelerograms (in terms of PGA) to irregular shear
 355 stress histories:

$$\tau_{eq}(t) = \frac{a(t)}{g} \times \sigma_{v,c} \times r_d \quad (8)$$

356

358 where $a(t)$ is the horizontal ground acceleration over time at the
 359 ground surface, generated by the earthquake.

$$CSR_{eq}(t) = \frac{\tau_{eq}(t)}{\sigma'_{v,c}} \quad (9)$$

360 The $CSR_{eq}(t)$ is the irregular shear stress history normalized by
 362 the total vertical effective stress.
 363

364 **Multichannel seismic reflection data acquisition and processing**

365 During the Poseidon cruise POS 500 in 2016, seismic data were
 366 acquired using the high-resolution multichannel seismic system from
 367 the Department of Geosciences of the University of Bremen (Kopf and
 368 Cruise Participants 2016). A Sercel Micro-GI-Gun with chamber vol-
 369 umes of 2×0.1 l yielding source frequencies of 80–400 Hz and a main
 370 frequency of 200 Hz, served as the seismic source. The acquisition
 371 system consisted of a 160-m-long Teledyne streamer with 64 channels.
 372 The seismic data has a vertical resolution of 2–4 m (Fig. 2). During
 373 post-processing, the data was common midpoint binned to 1 m, thus
 374 maximizing lateral resolution of the data. Fold of the data, i.e., the
 375 number of traces per bin, is usually 6–8. Furthermore, the data was
 376 bandpass-filtered, NMO-corrected using interactively picked velocity
 377 fields, CMP-stacked and migrated. For processing, the Vista Seismic
 378 Processing Software (Schlumberger) was used while interpretation was
 379 carried out in Kingdom (IHS). During interpretation, reflectors were

picked semi-automatically, gridded and isochore maps were calculat- 380
 ed. Volumes were calculated for individual seismic units within a 381
 defined area. 382

Results 383

Slope geometry offshore Nice 384

The multichannel seismic reflection data shows the general reflection 385
 pattern of the Nice shelf area with gently seaward dipping strata (Fig. 386
 2). Three horizons were picked, the lowermost Reflector 1 (R1) is the 387
 upper boundary of a set of low-frequency discontinuous reflector 388
 segments of medium amplitude that generally dip seaward (Fig. 2a). 389
 This surface is believed to be of Pliocene age and to consist of 390
 conglomerates (Auffret et al. 1982). Reflector 2 (R2) was mapped 391
 over most of the shelf area east of the 1979 landslide scar (Fig. 3). It 392
 is a medium amplitude continuous seaward-dipping reflector at a 393
 depth of less than 10 mbsf on the shelf and ~ 25 mbsf at the shelf 394
 edge. On the shelf, it lies almost horizontal while towards the shelf 395
 edge it dips seaward at $> 8^\circ$. At its seaward termination, it is trun- 396
 cated by the seafloor, indicating mass wasting scars at the upper 397
 slope. Between R1 and R2, only few reflectors are observed due to the 398
 presence of strong multiple reflections. However, the reflector pat- 399
 tern shows parallel to sub-parallel seaward-dipping reflectors below 400
 R2 at the shelf edge. Reflector 3 (R3) was mapped mostly on the outer 401
 shelf area (Fig. 2a) and is a continuous high amplitude reflector that 402
 terminates against the seafloor at its seaward termination as well as 403
 towards the shore. Its maximum depth lies, similarly to R2, on the 404
 outer shelf. 405

Both R2 and R3 correspond to layers of increased cone resistance in the CPTu 406
 profile PFM 11-S6 in Fig. 2b. Further, CPTu 407
 profiles are well correlated with the picked R2 and R3 reflectors 408
 (CPTu locations in Fig. 1a). While the high-amplitude R3 409

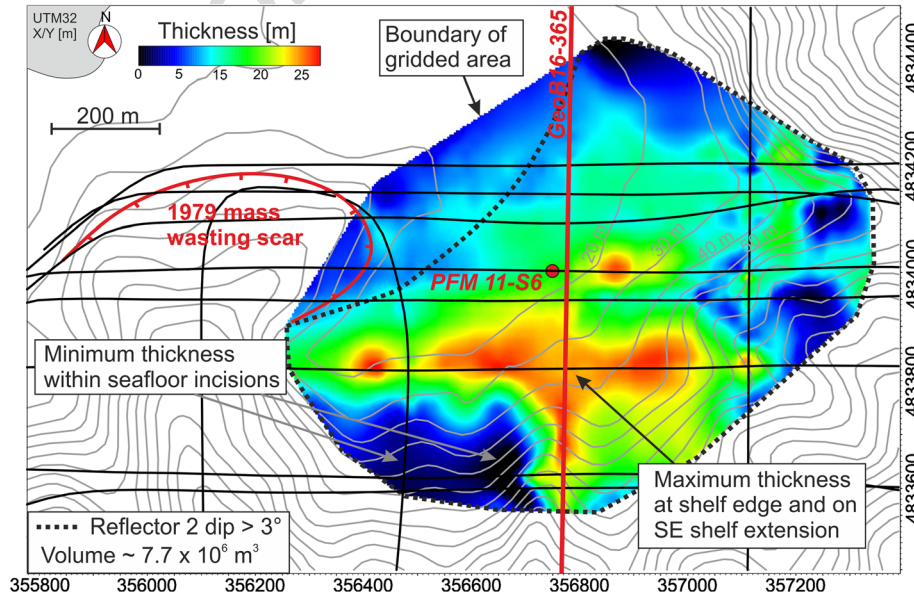


Fig. 3 Thickness map of the seismic unit between R2 and the seafloor. The gridding of horizons and thickness calculations were restricted to an area of interest on the shelf east of the 1979 mass wasting scar. Black lines indicate seismic profiles used for reflector mapping (see Fig. 2). Contour lines are calculated from the bathymetry shown in Fig. 1

410 corresponds to the second highest peak in the CPTu profile, the
 411 medium-amplitude R2 coincides with the overall maximum of the
 412 CPTu measurement.

413 The number of multichannel seismic profiles in the study area
 414 (Fig. 3) allowed us to map R2 on most of the shelf area. Figure 3
 415 shows the thickness of the seismic unit between R2 and the
 416 seafloor, comprising most of the visible seaward-dipping shelf
 417 strata in our data. The picked horizon was gridded within the area
 418 of interest on the shelf east of the 1979 landslide scar. An isochore
 419 map was calculated using the picks of R2 and the seafloor which
 420 was subsequently time-depth converted using a velocity of
 421 1600 m s^{-1} . The above-described profile GeoB16-365 is representa-
 422 tive for the mapped unit. Hence, the thickness of the mapped unit
 423 varies between 0 and ~ 25 mbsf and its maximum thickness is
 424 located at the shelf edge while the thickness gradually decreases
 425 landwards (Fig. 3). At the upper slope, the unit thickness drops
 426 abruptly to zero in several places, usually coinciding with V-
 427 shaped seafloor incisions (Fig. 3). Kelner et al. (2016) analyzed
 428 these seafloor incisions in detail and described them as small
 429 landslide scars. The volume of the mapped unit was calculated in
 430 the area of interest where the dip of R2 exceeds 3° . We chose 3° as
 431 a threshold value because this slope angle is typical for submarine
 432 landslide source areas (Hühnerbach and Masson 2004). The
 433 mapped volume comprises $\sim 7.7 \times 10^6 \text{ m}^3$. This volume lies in
 434 water depths between 20 and 80 m and focuses on the remnant
 435 shelf area towards the SE of the gridded area.

436 **Geotechnical index properties and direct shear testing**

437 The coarse-grained sediment layers in core KS07 and KS06 consist of
 438 clay, silt, and sand (Fig. 4). According to the Shepard classification
 439 scheme (Shepard 1954), all samples are silty sand or sandy silt. For
 440 our study, we regarded all samples as similar. We chose the sample
 441 KS07_215cm with an intermediate grain size diameter at 50% cumu-
 442 lative grain size to derive index and mechanical parameters (inset in

Fig. 4). The Atterberg limits show that our sediment is classified as
 low plastic clay with a liquid limit of 31% (inset in Fig. 4) (BS
 5930:1999 + A2:2010 1999). The shear stress curves of the direct shear
 tests for initially loose sandy silt have not distinct peak and yield an
 effective critical angle of internal friction of 33° (Fig. 5a).

Uniform triaxial shear testing and factor of safety analysis

The test results of the uniform cyclic triaxial shear tests are
 presented as a function of loading cycles (Fig. 6a). Figure 6a
 exemplarily shows the evolution of the CSR_{cyc} , the pore pressure
 ratio r_u , and the axial strain with increasing number of loading
 cycles of a uniform cyclic triaxial test on a reconstituted sample
 sheared at a cyclic shear stress ratio CSR_{cyc} of 0.2. The pore
 pressure ratio increases with each loading cycle until it reaches
 unity and the sample is liquefied. The axial strain follows the
 typical pattern of cyclic triaxial tests on granular materials
 (Castro 1969). During the first four cycles, there is no significant
 strain. Only with increasing pore water pressure and hence de-
 creasing effective stress, the sample deforms substantially. The
 primary outcome of such tests is the number of cycles a sample
 can bear at a given CSR_{cyc} (Table 1). The sample needs at small
 CSR_{cyc} a large number of cycles to failure, whereas large CSR_{cyc}
 cause failure in a few loading cycles. We evaluated the influence of
 structure and fabric of an undisturbed sample on cyclic shear
 strength by comparing a core sample with a reconstituted sample
 at the same CSR_{cyc} (Fig. 6b). Both samples show very similar pore
 water pressure and deformation response. Thus, the number of
 cycles to failure was the same in both tests, but the two samples
 had different void ratios (Table 1). The reconstituted and the core
 sample had a void ratio of 0.71 and 0.96, respectively.

The sediment cyclic strength curve based on the $CRR_{0.9}$ and number
 of cycles to failure is very well described by a power law function
 (Fig. 6b). This cyclic strength curve separates the plot into two areas:
 one above the line indicating unstable conditions and one below the
 line indicating stable conditions. A converted arbitrary loading signal
 that plots above the cyclic strength curve signifies that the earthquake-
 induced shear stresses are larger than the resistance of the samples and
 vice versa. All CSRs derived from the simulated accelerograms plot
 above the cyclic strength curve, in the unstable field. The median PGA
 of all 500 simulations conducted by Salichon et al. (2010) is shown by a
 square, whereas the range between the 16th and 84th percentiles
 representing $\sim 66\%$ of all 500 simulations. Hence, the factor of safety
 against liquefaction for all simulations is < 1 , which indicates sediment
 failure in the tested scenario. The Mw 6.3 earthquake with a median
 PGA results in a factor of safety of 0.58 and the minimum simulated
 PGA results in a factor of safety of 0.95. The seismic demand of a Mw
 6.5 earthquake which Sultan et al. (2004) considered in their geotechni-
 cal analysis, plot in the stable field below the cyclic strength curve in
 Fig. 6b which is related to the consideration of lower PGA values than
 simulated by Salichon et al. (2010).

Arbitrary triaxial shear test

The CSR_{eq} , r_u , and axial strain of arbitrary loading tests are pre-
 sented as a function of time in Fig. 7. Figure 7a shows the exper-
 imental results from the simulated accelerogram corresponding to
 the 16th percentile in terms of maximum shear stress (Fig. 6b)
 (Salichon et al. 2010). In general, the DTTD is able to respond to
 the requested earthquake input signal; however, during the major
 loading period in some cases, the response function reached only

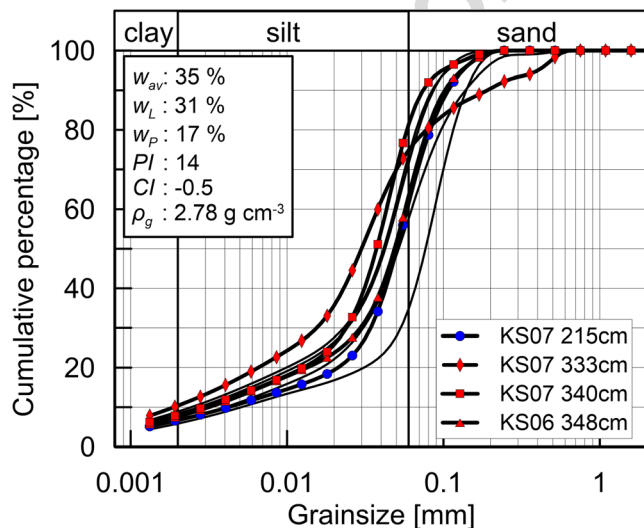


Fig. 4 Cumulative grain size distribution curves for KS06 and KS07 samples. Red squares/triangles/diamonds show triaxial test samples, whereas the blue dots represent direct shear test and Atterberg samples. w_{av} —average water content of sandy silt layers, w_L —liquid limit, w_P —plastic limit, PI —plasticity index, CI —consistency index, ρ_g —grain density

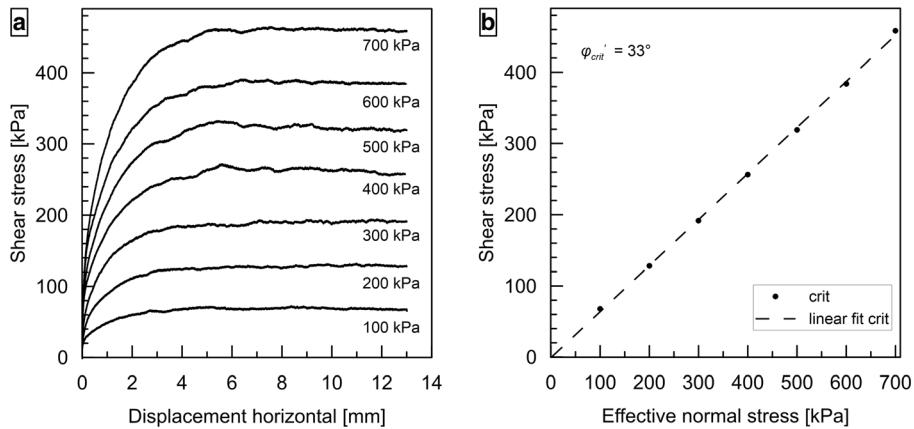


Fig. 5 a Direct shear test results of sample KS07_215cm. Numbers indicate normal stress. b Shear plane

up to 65% of the peak stress (inset in Fig. 7a). We measured a pore water pressure response immediately after loading starts; yet, we first detected a significant pore water pressure increase at a CSR_{eq} threshold of 0.1. The rapid increase of pore water pressure corresponds to the largest shear stresses induced by the largest accelerations. Significant deformation occurs simultaneously. The complete earthquake signal produced an excess pore pressure ratio of approximately 85%. However, an astonishing result is that the pore water pressure kept rising by 15% after the major loading pulse (10–18 s) had subsided. We reached initial liquefaction approximately 9 min after earthquake loading stopped. The second test (Fig. 7b) is based on the accelerogram with the minimum PGA out of 500 simulations (Salichon et al. 2010). Hence, it is comparable with the minimum CSR in Fig. 6b. In a few cases, the response function reached only up to 85% of the peak stress (inset in Fig. 7b). During loading, the pore pressure ratio increased to 30%. Simultaneously, the axial strain reaches 0.25%. Neither initial liquefaction nor significant axial strain occurred in this test.

During that test, we were not aware of the possible post-loading pore water pressure rise, which is why we stopped recording.

Discussion

Sample material and stress conditions

The geotechnical behavior of sandy silt is in general, not well understood, because its behavior is neither like a perfectly granular sediment as sand nor like cohesive sediment as clay. Many studies analyze cyclic behavior of either granular or cohesive sediments, but very little is known about the behavior of marine sandy silt deposits under cyclic loading. The sandy silt in this study shows characteristics of both granular sediment with $\phi'_{crit} = 33^\circ$ (Sadrekarimi and Olson 2011) and cohesive sediment by having Atterberg limits. Based on the index properties, the tested sediment cannot be characterized unambiguously as susceptible or non-susceptible to liquefaction. Whether or not a sediment type is susceptible to liquefaction may be estimated

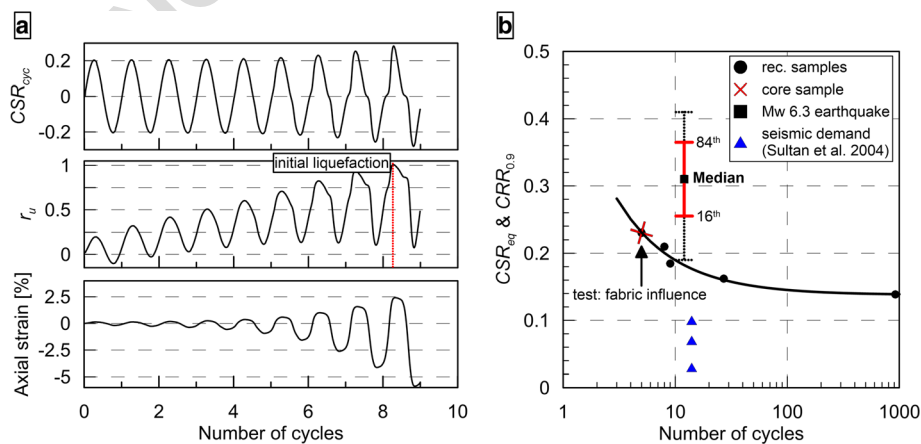


Fig. 6 a Undrained uniform cyclic triaxial test results of test U3. From top to bottom: uniform loading function, excess pore pressure ratio, and axial strain. Red dashed line indicates initial liquefaction. b CSR_{eq} and $CRR_{0.9}$ versus number of cycles to failure shows the cyclic strength curve and the CSR range of the modeled earthquake. The square indicates the CSR_{eq} derived from the median PGA published by Salichon et al. (2010), whereas the black dotted line presents the CSR range based on all 500 simulations and the red thick line present the 16th to 84th percentile of the 500 simulations. The blue triangles present the seismic demands of a Mw 6.5 earthquake used in the geotechnical study by Sultan et al. (2004)

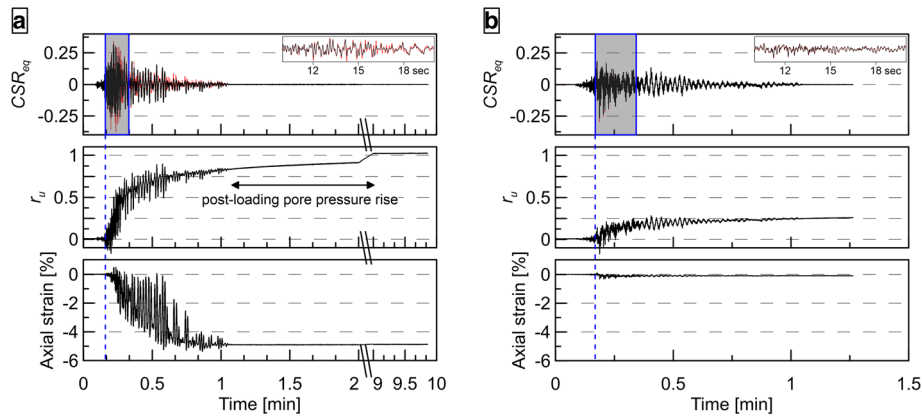


Fig. 7 a Undrained arbitrary triaxial test results of the 16th percentile modeled PGA earthquake. b Minimum modeled PGA earthquake. Top to bottom: input function (red dashed lines) and DTTD response function (black line); excess pore pressure ratio, axial strain. Y-axis scale of a and b are the same to illustrate differences between the tests. Insets show zoom of major loading period (shaded area). Blue dashed line illustrates CSR_{eq} threshold

534 from the Atterberg limits (Boulanger and Idriss 2006; Bray and
 535 Sancio 2006). After Boulanger and Idriss (2006), our samples
 536 are characterized as clay-like and non-susceptible to liquefac-
 537 tion. In contrast, after Bray and Sancio (2006), the samples of
 538 our study would be moderately susceptible. Our cyclic triaxial
 539 test results clearly document the liquefaction potential of the
 540 tested sediment and thereby highlight the necessity of such
 541 sophisticated testing procedures.

542 The effective normal stress in the triaxial tests was chosen based
 543 on CPTu and shallow water reflection seismic data. From the CPTu
 544 data, the high and medium amplitudes of R3 and R2 may be
 545 interpreted as coarse-grained sediments within the generally
 546 fine-grained clay-to-silt deposits of the study area (Kopf et al.
 547 2016; Sultan et al. 2010). Both reflectors represent coarse-grained
 548 sediments in contrast to the surrounding sediment. Close to the
 549 shelf edge, R2 has an average depth of ~ 23 mbsf, which translates
 550 to 170 kPa vertical effective stress (appendix Table 2). Hence, in
 551 this study, we assume that coarse-grained sediment layers identi-
 552 fied as peaks in CPTu data and strong reflectors in seismic
 553 profiles are similar to coarse-grained sediments found in ~ 5 -m-
 554 long Kullenberg cores further upslope. This assumption can be
 555 made due to two facts: (1) the early to middle Holocene sedimen-
 556 tation pattern is characterized by a gap in gravel supply to the Var
 557 river mouth. Hence, silt and sand are the coarsest sediment sup-
 558 plied to the Var delta (Dubar and Anthony 1995). (2) This is
 559 confirmed by the longest core (17 m) MD01-2470 ever taken on
 560 the Nice submarine slope (Dan 2007). MD01-2470 shows sedimen-
 561 tary layers of clay and silty clay with recurring interbeds of silt and
 562 sometimes sand. Following seismic stratigraphy interpretation,
 563 these coarse-grained layers are seaward-dipping and are deepening
 564 with increasing distance from shore.

565 Huang et al. (2012) showed that cyclic resistance of the soil
 566 decreases with lower effective confining stress. Consequently, the
 567 granular layers in shallower depth, e.g., R3 or our cored sediments,
 568 would most likely liquefy under even smaller PGAs. By choosing a
 569 confining stress reigning at 23 mbsf, we present a worst-case
 570 scenario since a sudden failure nucleating at that depth is more
 571 likely to create a tsunami than a failure at 5 mbsf because of the
 572 larger slide volume.

573 It is well known that sample preparation affects the cyclic
 574 strength of sediments and that reconstituted samples are mostly
 575 less resistant than undisturbed samples (Idriss and Boulanger
 576 2008; Mulilis et al. 1977). Structure and fabric are relevant for
 577 sediment strength. Remolding completely destroys the natural
 578 structure and fabric of a sediment sample. Yet, the reconstituted
 579 sample U5 and the core sample U6 failed after five cycles under
 580 identical loading amplitudes. Intuitively, we would expect the
 581 reconstituted sample to fail after fewer cycles than the core
 582 sample. However, the different void ratios of the samples may
 583 explain our results. The liquefaction resistance is closely linked
 584 to the void ratio of a sediment sample; the looser the sample the
 585 easier it is to liquefy (Kramer 1996). The core sample shows a
 586 higher void ratio than the reconstituted sample and is thus
 587 expected to be more prone to liquefaction. The similar mea-
 588 sured liquefaction resistance of the reconstituted sample U5 and
 589 the mostly intact sample U6 may indicate that the looser state
 590 compensates the higher strength from intact fabric and struc-
 591 ture. All cyclic uniform triaxial test samples after consolidation
 592 have a void ratio of 0.73 ± 0.06 , which is significantly lower than
 593 the void ratios of the three core samples of 0.99 ± 0.03 . The in
 594 situ void ratio in ~ 23 mbsf is unknown. However, the compar-
 595 ison of the core samples U6 and the reconstituted sample U5,
 596 both consolidated to the overburden stress reigning at ~ 23 mbsf,
 597 indicates that strength related to structure and fabric is com-
 598 pensated by lower void ratios in reconstituted samples. Hence,
 599 we tentatively assume that the cyclic strength curve ($R^2 = 0.96$)
 600 in Fig. 6b, which results from tests on reconstituted samples, is
 601 similar to a curve resulting from tests on undisturbed samples.

Nice seismogenic slope stability

602 The spatially widespread coarse-grained sediment layers are dip-
 603 ping seawards and are partly cut by some older slide scars. If a
 604 Mw 6.3 earthquake were to occur 25 km offshore, the sandy silt
 605 layers will liquefy and lose its entire shear strength. Since there is
 606 no backstop and since sediment has no tensile strength, a slope
 607 failure with a volume of $\sim 7.7 \times 10^6$ m³ would be the result. The
 608 volume is $\sim 11\%$ smaller than the initial 1979 slide volume calcu-
 609 lated from differential bathymetry by Assier-Rzadkiewicz et al.
 610

611 (2000) and ~23% smaller than the proposed volume by Labbé
 612 et al. (2012). Shallow water depth of 20–80 mbsl favors dangerous
 613 tsunamis (Harbitz et al. 2006). Labbé et al. (2012) and Assier-
 614 Rzdakieaicz et al. (2000) modeled the 1979 landslide as a flow of a
 615 viscous fluid with a medium viscosity. If the slide parameters
 616 regarding volume, slide geometry, viscosity, and water depth for
 617 a potential earthquake triggered submarine landslide would be
 618 similar, we speculate that a local tsunami comparable in size to
 619 the 1979 tsunami is possible even though the trigger mechanism
 620 of the two slides clearly differ.

621 The slope stability analysis presented in Sultan et al. (2004) is
 622 based on cyclic triaxial tests similar to the ones conducted in this
 623 study. The triaxial test results by Sultan et al. (2004) show a
 624 higher soil cyclic resistance compared to this study. However, the
 625 sample preparation, the sample dimensions, confining stresses,
 626 and void ratios of the samples are not documented. Further-
 627 more, earthquake details such as, e.g., site-source distance, are
 628 missing. Thus, it is unfortunately not possible to compare our
 629 triaxial test results with those published by Sultan et al. (2004) in
 630 satisfactory detail. Moreover, the PGAs considered in their study
 631 are only approximately 25% of the median PGA (NALS) pub-
 632 lished by Salichon et al. (2010), which certainly means that these
 633 authors have not taken into account the site effects. Therefore,
 634 their results certainly overestimate the factor of safety. Our study
 635 considers an offshore Mw 6.3 earthquake causing high PGAs at
 636 station NALS within the city of Nice. At the time of the labora-
 637 tory study, only data from the stations published in Salichon
 638 et al. (2010) were available, and therefore, station NALS was
 639 chosen as a reference station due to its proximity to the studied
 640 area and its geological setting. In October 2016, a new permanent
 641 broad band seismometer (PRIMA) has been installed offshore
 642 Nice on the shallow submarine slope at a depth of 17 mbsf. Data
 643 from the station is freely available through the RESIF Seismic
 644 data portal (<http://seismology.resif.fr/>). A first analysis of a few
 645 local earthquakes recorded at the station will be published soon
 646 by F. Courboux and colleagues. Based on this new data, we
 647 know that the ground motions recorded at station NALS are
 648 similar to the one at PRIMA station. Hence, our initial
 649 assumption is valid most likely because the site conditions are
 650 almost identical. Furthermore, the ground motions resulting
 651 from the rupture of the fault considered in Salichon et al.
 652 (2010) are not the only potential source for large PGAs at the
 653 shallow submarine Nice slope. A potential Mw 5.7 earthquake on
 654 the Blausasc fault north-east of Nice would also cause high PGAs
 655 ($> 1.5 \text{ m s}^{-2}$) in the city of Nice (Courboux et al. 2007) and may
 656 therefore also act as a trigger for a tsunamigenic submarine
 657 slope failure offshore Nice.

658 Liquefaction under arbitrary loading

659 First steps were taken to simulate arbitrary earthquake motions
 660 with the DTTD on core samples. The uniform tests indicate lique-
 661 faction for the full range of ground motions. In contrast, the
 662 arbitrary loaded test samples liquefied under 16th percentile ac-
 663 celeration in terms of all modeled PGAs but not under the mini-
 664 mum modeled PGA. However, the accumulated load of the
 665 earthquake input function is larger than the actual load subjected
 666 to the sample, because of limits of the DTTD (insets in Fig. 7). This
 667 discrepancy could explain the different results between uniform
 668 and arbitrary tests.

The ‘delayed liquefaction’ 9 min after loading with the 16th
 percentile PGA accelerogram is probably caused by localized
 liquefaction and slow seepage of the excess pore water pressure
 through relatively low permeable sediment to the sensor. Seep-
 age is needed to transfer the pressure because of the compress-
 ibility of the sensor, the tubing and possibly some small air
 bubbles in the pores. The localization of the liquefaction may
 be caused by natural heterogeneity of the core sample, and
 localization in the central part is additionally promoted by the
 stabilization of the sample by friction at the sinter metal filters
 at the top and bottom of the sample. Other laboratory studies
 have directly measured localized pore water pressure rise in the
 shear zone (Thakur 2007).

Delayed pore water pressure rise or increased permeability in
 the field is probably the cause for landslides occurring minutes to
 days after earthquake loading at a quiet time without any tremor
 (Holzer et al. 1989; Ishihara 1984; Jibson et al. 1994). Post-
 earthquake pore water pressure rise was first observed at a field
 liquefaction experiment by Holzer et al. (1989); they explained the
 delay in pore water pressure rise by pore water pressure redistri-
 bution in the sediment. In natural slopes, it is probably the mate-
 rial heterogeneity and differences in loading which lead to
 localized pore water pressure rise, but to some extent is the
 ‘delayed liquefaction’ after the arbitrary triaxial loading test an
 analog to delayed failure after earthquake loading. Nevertheless,
 differences between arbitrary and uniform loading need further
 investigation and testing.

696 Conclusions

697 Several authors pointed out the likelihood of Mw ~6 earth-
 698 quakes around the city of Nice (Courboux et al. 2007;
 699 Salichon et al. 2010). These earthquakes may generate large
 700 ground motions on alluvial Quaternary fillings, which may be
 701 much greater than those considered in earlier studies. Based on
 702 our study, we conclude that coarse-grained Quaternary sedi-
 703 ment layers of the Var delta are prone to liquefaction during
 704 an Mw 6.3 earthquake produced 25 km offshore Nice. From
 705 uniform cyclic triaxial tests, we calculate a factor of safety
 706 against liquefaction < 1 for the Nice submarine slope sediments.
 707 Liquefied sediment may cause a slope failure similar in size to
 708 the 1979 event. Consequently, a local tsunami along the Nice
 709 coast is possible in the herein conceived scenario. The arbitrary
 710 tests are an innovative pilot study that leads to pore water
 711 pressure signals similar to observations made in the field. The
 712 observed post-loading pore water pressure rise is probably re-
 713 lated to pore water pressure redistribution in the sample and is
 714 a potential slope failure triggering mechanism.

715 Acknowledgements

716 We thank our French colleagues from the “Institut français de
 717 recherche pour l’exploitation de la mer” for coring during their
 718 STEP 2015 oceanographic cruise DOI [https://doi.org/10.17600/](https://doi.org/10.17600/15006100)
 719 [15006100](https://doi.org/10.17600/15006100) on the research vessel L’Europe. Additionally, we thank
 720 the crew and scientists on board Poseidon cruise POS 500 for the
 721 seismic data acquisition. Moreover, we would like to thank Prof.
 722 Tobias Mörz for providing triaxial testing cells. Matthias Lange is
 723 thanked in memoriam for outstanding technical assistance with
 724 the DTTD. David Völker is thanked for fruitful discussions while
 725 working on this manuscript. We would like to thank Schlumberger
 726

727 and IHS for providing academic licenses for Vista Seismic Process-
728 ing Software and Kingdom respectively.

729
730
731 **Funding information**

732 This work was supported by the “Deutsche Forschungsgemeinschaft”
733 via MARUM Research Center (Grants FZT15 and EXC309) in the area
734 Seafloor Dynamics. **Appendix**

735 **Materials and methods**

736 **Cyclic Shear Stress**

737 Any arbitrary earthquake signal can be translated into a uni-
738 form cyclic loading signal defined by a CSR_{eq} and an equivalent
739 number of uniform cycles (Cetin and Seed 2004; Liu et al. 2001;
740 Seed and Idriss 1971). The maximum cyclic shear stress was
741 calculated at ~ 23 mbsf. The total vertical stress was calculated
742 with an average bulk density of 1800kgm^{-3} , which is represen-
743 tative for the slope sediments (Kopf and Cruise Participants
744 2008), and a Mediterranean water density of 1035kgm^{-3} . The
745 stress reduction factor accounts for the damping of the soil as
746 an elastic body (Seed and Idriss 1971). Thus, it considers the
747 variation of cyclic shear stresses with depth and was calculated
748 according to a modified equation after Cetin and Seed (2004).
749 The stress reduction factor is based on four descriptive
750 variables:
751

$$r_d = \left(\frac{1 + \frac{-23.013 - 2.949 \times a_{max} + 0.999 \times M_w + 0.0525 \times V_{s12m}}{16.258 + 0.201 \times e^{0.341 \times (-20 + 0.0785 \times V_{s12m} + 7.586)}}}{1 + \frac{-23.013 - 2.949 \times a_{max} + 0.999 \times M_w + 0.0525 \times V_{s12m}}{16.258 + 0.201 \times e^{0.341 \times (0.0785 \times V_{s12m} + 7.586)}}} \right) - 0.0046 \times (d - 20) \quad (10)$$

753
754 where a_{max} is the peak ground acceleration, d is the depth of the
755 sediment, V_{s12m} is the mean shear wave velocity in the upper 12m
756 of sediment, and M_w is the moment magnitude of the earthquake.
757 Table 2 summarizes our input parameters to calculate the seismic
758 demand (in terms of cyclic shear stress) at depth.

759 The cyclic shear stress is induced by cyclic vertical loading
760 and unloading on a cylindrical sediment sample at constant

lateral stress. The maximum cyclic shear stress τ_{cyc} in the triaxial
sample is:

$$\tau_{cyc} = \frac{q_{cyc}}{2} \quad (11)$$

The samples were loaded in harmonic compression-extension
mode (i.e., $q_{min} < 0 < q_{max}$ and $|q_{min}| = |q_{max}|$). The loading signal
was applied with a frequency of 1Hz. Both the loading pattern and
the loading frequency are standards in earthquake engineering
(ASTM Standard D5311/D5311M – 13 2013; Kramer 1996). The verti-
cal displacement, principle stresses, deviator stress, and excess
pore water pressure were recorded at 100Hz during cyclic loading.
Prior to each experiment, the samples were vacuum saturated to a
Skempton B-value ≥ 0.92 (Skempton 1954) with deionized,
deaerated water.

Seismic waves passing a sediment are associated with complex
strain and stress paths near the ground surface, where the princi-
ple stresses change in direction and magnitude (El Shamy and
Abdelhamid 2017). Thus, Seed et al. (1978) investigated the impact
of multidirectional loading conditions and suggested a strength
reduction factor of 10% for uniaxial loading. We corrected the CRR
by 10% to account for the unidirectional loading during the triax-
ial tests.

$$CRR_{0.9} = CRR \times 0.9 \quad (12)$$

785 **Sample Preparation**

786 Most triaxial tests were conducted on reconstituted samples (of
787 the original sediment) to make sure that (i) there are no mineral-
788 ological differences from one sample to another, (ii) the samples are
789 homogenous, and (iii) we could perform as many tests as needed
790 without running out of sample material. Reconstituted samples
791 were prepared from a slurry following the approach from
792 Bradshaw and Baxter (2007). The samples were prepared by
793 mixing soil and water to a slurry with a water content of 33%,
794 which is 2% higher than the liquid limit (Fig. 4). The slurry was
795 filled in a cylindrical mold and tamped to remove air bubbles. The
796 samples were one-dimensionally pre-consolidated to 100kPa verti-
797 cal stress. After pre-consolidation, the samples were set up in the
798 triaxial cell and vacuum saturated for at least 2h. In the DTTD, the
799 samples were isotopically consolidated, with a ramp sufficient

t2.1 **Table 2** Input variables to calculate the seismic demand at a soil layer at ~ 23 mbsf for different PGAs of a modeled Mw 6.3 earthquake

a_{max}	3.1–4.6–5.8–7.5–12.1 m s^{-2} (minimum–16th–median–84th–maximum)	t2.2
g	9.81 m s^{-2}	t2.3
$\sigma'_{v,c}$	~ 400 kPa	t2.4
	bulk density: 1800 kg m^{-3}	t2.5
	depth: ~ 23 mbsf	t2.6
	~ 170 kPa	t2.7
r_d	water density: 1035 kg m^{-3}	t2.8
	depth: ~ 23 mbsf	t2.9
	0.40, 0.37, 0.35, 0.32, 0.22	V_{s12m} : 140 m s^{-1} depth: ~ 23 mbsf

800 small to allow the sample to drain, to an effective confining stress
 801 of 170kPa. This sample preparation procedure allowed us to create
 802 comparable homogenous samples with a small scatter in void
 803 ratios (Table 1):

$$e = \frac{V_V}{V_S} \quad (13)$$

804 where V_V is the volume of voids and V_S is the volume of solids.

805 In contrast, core samples were carefully extracted from the core
 806 via a metal cylinder to maintain the in situ fabric as good as
 807 possible. We used for core and reconstituted samples the same
 808 consolidation procedure. By comparing core and reconstituted
 809 samples under identical loading conditions, the influence of
 810 remolding on the cyclic shear strength was evaluated.
 811
 812

813 References

814 Agrawal YC, McCave IN, Riley JB (1991) Laser diffraction size analysis. In: Syvitski JPM
 815 (ed) Principles, methods, and application of particle size analysis. Cambridge Univer-
 816 sity Press, Cambridge, pp 119–128
 817 Ai F, Förster A, Stegmann S, Kopf A (2014) Geotechnical characteristics and slope stability
 818 analysis on the deeper slope of the Ligurian margin, southern France. In: Sassa K (ed)
 819 Landslide science for a safer geoenvironment. Springer, Cham, pp 549–555
 820 Anthony EJ (2007) Problems of hazard perception on the steep, urbanised Var coastal
 821 floodplain and delta, French Riviera. *Méditerranée*:91–97. doi: [https://doi.org/](https://doi.org/10.4000/mediterranee.180)
 822 [10.4000/mediterranee.180](https://doi.org/10.4000/mediterranee.180)
 823 Anthony EJ, Julian M (1997) The 1979 Var delta landslide on the French Riviera: a
 824 retrospective analysis. *J Coast Res* 13:27–35
 825 Assier-Rzadkiewicz S, Heinrich P, Sabatier PC, Savoye B, Bourillet JF (2000) Numerical
 826 modelling of a landslide-generated tsunami: the 1979 Nice event. *Pure Appl Geophys*
 827 157:1707–1727. <https://doi.org/10.1007/PL00001057>
 828 ASTM Standard D5311/D5311M – 13 (2013) Test method for load controlled cyclic
 829 triaxial strength of soil
 830 Auffret GA, Auzende JM, Gennesseaux M, Monti S, Pastouret L, Pautot G, Vanney JR
 831 (1982) Recent mass wasting processes on the Provençal margin (western Mediterra-
 832 nean). In: Saxov S, Nieuwenhuis JK (eds) Marine slides and other mass movements.
 833 Springer, Boston, pp 53–58
 834 Boulanger RW, Idriss IM (2006) Liquefaction susceptibility criteria for silts and clays. *J*
 835 *Geotech Geoenviron* 132:1413–1426. [https://doi.org/10.1061/\(ASCE\)1090-](https://doi.org/10.1061/(ASCE)1090-0241(2006)132:11(1413))
 836 [0241\(2006\)132:11\(1413\)](https://doi.org/10.1061/(ASCE)1090-0241(2006)132:11(1413))
 837 Bradshaw AS, Baxter CDP (2007) Sample preparation of silts for liquefaction testing.
 838 *Geotech Test J* 30:324–332. <https://doi.org/10.1520/GTJ100206>
 839 Bray JD, Sancio RB (2006) Assessment of the liquefaction susceptibility of fine-grained
 840 soils. *J Geotech Geoenviron* 132:1165–1177. [https://doi.org/10.1061/\(ASCE\)1090-](https://doi.org/10.1061/(ASCE)1090-0241(2006)132:9(1165))
 841 [0241\(2006\)132:9\(1165\)](https://doi.org/10.1061/(ASCE)1090-0241(2006)132:9(1165))
 842 BS 1377–2:1990 (1990) Methods of test for soils for civil engineering purposes - part 2:
 843 classification tests. **British Standard Institution**, London
 844 BS 5930:1999+A2:2010 (1999) Code of practice for site investigations. **British Stan-**
 845 **dard Institution**, London
 846 Castro G (1969) Liquefaction of sands: Dissertation. Harvard Soil Mechanics Series, vol 87.
 847 Harvard University, Cambridge, Massachusetts
 848 Cavalié O, Sladen A, Kelner M (2015) Detailed quantification of delta subsidence,
 849 compaction and interaction with man-made structures: the case of the NCA airport,
 850 France. *Nat Hazards Earth Syst Sci* 15:1973–1984. [https://doi.org/10.5194/nhess-15-](https://doi.org/10.5194/nhess-15-1973-2015)
 851 [1973-2015](https://doi.org/10.5194/nhess-15-1973-2015)
 852 Cetin OK, Seed RB (2004) Nonlinear shear mass participation factor (rd) for cyclic shear
 853 stress ratio evaluation. *Soil Dyn Earthq Eng* 24:103–113. [https://doi.org/10.1016/](https://doi.org/10.1016/j.soildyn.2003.10.008)
 854 [j.soildyn.2003.10.008](https://doi.org/10.1016/j.soildyn.2003.10.008)
 855 Cochonot P, Bourillet JF, Savoye B, Dodd L (1993) Geotechnical characteristics and
 856 instability of submarine slope sediments, the Nice slope (N-W Mediterranean Sea).
 857 *Mar Georesour Geotechnol* 11:131–151. <https://doi.org/10.1080/10641199309379912>
 858 Courboux F, Larroque C, Deschamps A, Kohrs-Sansorny C, Gélis C, Got JL, Charreau J,
 859 Stéphan JF, Béthoux N, Virieux J, Brunel D, Maron C, Duval AM, Perez J-L, Mondelli P
 860 (2007) Seismic hazard on the French Riviera: observations, interpretations and

simulations. *Geophys J Int* 170:387–400. [https://doi.org/10.1111/j.1365-](https://doi.org/10.1111/j.1365-246X.2007.03456.x)
 246X.2007.03456.x
 Dan G (2007) Processus gravitaires et evaluation de la stabilité des pentes: Approches
 géologiques et géotechnique: Dissertation. University Bretagne occidentale, Brest
 Dan G, Sultan N, Savoye B (2007) The 1979 Nice harbour catastrophe revisited: trigger
 mechanism inferred from geotechnical measurements and numerical modelling. *Mar*
Geol 245:40–64. <https://doi.org/10.1016/j.margeo.2007.06.011>
 DIN 18137-3 (2002) Baugrund, Untersuchung von Bodenproben - Bestimmung der
 Scherfestigkeit - Teil. Direkter Scherversuch. Deutsches Institut für Normung, Berlin, p 3
 Dubar M, Anthony EJ (1995) Holocene environmental change and river-mouth sedimenta-
 tion in the Baie des Anges, French Riviera. *Quat Res* 43:329–343. [https://doi.org/](https://doi.org/10.1006/qres.1995.1039)
 10.1006/qres.1995.1039
 El Shamy U, Abdelhamid Y (2017) Some aspects of the impact of multidirectional shaking
 on liquefaction of level and sloping granular deposits. *J Eng Mech* 143:C4016003–1–
 C4016003–17. [https://doi.org/10.1061/\(ASCE\)EM.1943-7889.0001049](https://doi.org/10.1061/(ASCE)EM.1943-7889.0001049)
 Ferrari G (1991) The 1887 Ligurian earthquake: a detailed study from contemporary
 scientific observations. *Tectonophysics* 193:131–139. [https://doi.org/10.1016/0040-](https://doi.org/10.1016/0040-1951(91)90194-W)
 1951(91)90194-W
 Gennesseaux M, Mauffret A, Pautot G (1980) Les glissements sous-marins de la pente
 continentale niçoise et la rupture de câbles en mer Ligure (Méditerranée occidentale).
 Comptes Rendus de l'Académie des Sciences de Paris 290:959–962
 Haque U, Blum P, da Silva PF, Andersen P, Pilz J, Chalov SR, Malet J-P, Auflič MJ, Andres
 N, Poyiadji E, Lamas PC, Zhang W, Peshevski I, Pétrusson HG, Kurt T, Dobrev N, García-
 Davaillo JC, Halkia M, Ferri S, Gaprindashvili G, Engström J, Keellings D (2016) Fatal
 landslides in Europe. *Landslides* 13:1545–1554. [https://doi.org/10.1007/s10346-016-](https://doi.org/10.1007/s10346-016-0689-3)
 0689-3
 Harbitz CB, Løvholt F, Pedersen G, Masson DG (2006) Mechanisms of tsunami generation
 by submarine landslides: a short review. *Nor J Geol* 86:255–264
 Holzer TL, Hanks TC, Youd TL (1989) Dynamics of liquefaction during the 1987
 Superstition Hills, California, earthquake. *Science* 244:56–59. [https://doi.org/](https://doi.org/10.1126/science.244.4900.56)
 10.1126/science.244.4900.56
 Honoré L, Courboux F, Souriau A (2011) Ground motion simulations of a major
 historical earthquake (1660) in the French Pyrenees using recent moderate size
 earthquakes. *Geophys J Int* 187:1001–1018. [https://doi.org/10.1111/j.1365-](https://doi.org/10.1111/j.1365-246X.2011.05193.x)
 246X.2011.05193.x
 Huang Y, Zheng H, Zhuang Z (2012) Seismic liquefaction analysis of a reservoir dam
 foundation in the south–north water diversion project in China. Part I: liquefaction
 potential assessment. *Nat Hazards* 60:1299–1311. [https://doi.org/10.1007/s11069-](https://doi.org/10.1007/s11069-011-9910-9)
 011-9910-9
 Hühnerbach V, Masson DG (2004) Landslides in the North Atlantic and its adjacent seas:
 an analysis of their morphology, setting and behaviour. *Mar Geol* 213:343–362.
<https://doi.org/10.1016/j.margeo.2004.10.013>
 Idriss IM, Boulanger RW (2008) Soil liquefaction during earthquakes. Engineering
 monographs on miscellaneous earthquake engineering topics, MNO-12. Earthquake
 Engineering Research Institute, Berkeley
 Ishihara K (1984) Post-earthquake failure of a tailings dam due to liquefaction of pond
 deposit. **International Conference on Case Histories in Geotechnical Engineering**
 Ishihara K (1985) Stability of natural deposits during earthquakes: 11th International
 conference on soil mechanics and foundation engineering. Proceedings, San
 Francisco, pp 321–376
 Jibson RW, Prentice CS, Borisoff BA, Rogozhin EA, Langer CJ (1994) Some observations
 of landslides triggered by the 29 April 1991 Racha earthquake, republic of Georgia.
Bull Seismol Soc Am 84:963–973
 Kelner M, Migeon S, Tric E, Courboux F, Dano A, Lebourg T, Taboada A (2016) Frequency
 and triggering of small-scale submarine landslides on decadal timescales: analysis of
 4D bathymetric data from the continental slope offshore Nice (France). *Mar Geol*
 379:281–297. <https://doi.org/10.1016/j.margeo.2016.06.009>
 Kodikara J, Seneviratne HN, Wijayakulasooriya CV (2006) Discussion of “using a small ring
 and a fall-cone to determine the plastic limit” by Tao-Wei Feng. *J Geotech Geoenviron*
 132:276–278. [https://doi.org/10.1061/\(ASCE\)1090-0241\(2006\)132:2\(276\)](https://doi.org/10.1061/(ASCE)1090-0241(2006)132:2(276))
 Kohrs-Sansorny C, Courboux F, Bour M, Deschamps A (2005) A two-stage method for
 ground-motion simulation using stochastic summation of small earthquakes. *Bull*
Seismol Soc Am 95:1387–1400. <https://doi.org/10.1785/0120040211>
 Kopf A, Cruise participants (2008) report and preliminary results of METEOR cruise M73/
 1: LIMA-LAMO (Ligurian margin landslide measurement & observatory), Cadiz
 22.07.2007 – Genoa 11.08.2007. Berichte aus dem Fachbereich Geowissenschaften
 der Universität Bremen
 Kopf A, Cruise Participants (2016) Report and preliminary results of R/V POSEIDON cruise
 POS 500, LISA, Ligurian slope AUV mapping, gravity coring and seismic reflection,
 930

931	Catania (Italy) – Malaga (Spain), 25.05.2016–09.06.2016. Berichte aus dem		Savoye B, Piper DJW (1991) The Messinian event on the margin of the Mediterranean		995
932	Fachbereich Geowissenschaften der Universität Bremen		Sea in the Nice area, southern France. <i>Mar Geol</i> 97:279–304. https://doi.org/10.1016/0025-3227(91)90121-J		996
933	Kopf A, Stegmann S, Garziglia S, Henry P, Dennielou B, Haas S, Weber K-C (2016) Soft		Savoye B, Piper DJW, Droz L (1993) Plio-Pleistocene evolution of the Var deep-sea fan off		997
934	sediment deformation in the shallow submarine slope off Nice (France) as a result of		the French Riviera. <i>Mar Pet Geol</i> 10:550–560. https://doi.org/10.1016/0264-8172(93)90059-2		998
935	a variably charged Pliocene aquifer and mass wasting processes. <i>Sediment Geol</i>		Seed BH, Idriss I (1971) Simplified procedure for evaluating soil liquefaction potential. <i>J</i>		999
936	344:290–309. https://doi.org/10.1016/j.sedgeo.2016.05.014		<i>Soil Mech Found Div</i> 97:1249–1273		1000
937	Kramer SL (1996) Geotechnical earthquake engineering. Prentice-hall international series		Seed BH, Pyke RM, Martin GR (1978) Effect of multidirectional shaking on pore pressure		1001
938	in civil engineering and engineering mechanics. Prentice Hall, Upper Saddle River, NJ		development in sands. <i>J Geotech Eng Div</i> 104:27–44		1002
939	Kreiter S, Moerz T, Strasser M, Lange M, Schunn W, Schlue BF, Otto D, Kopf A (2010)		Semblat J-F, Duval A-M, Dangla P (2000) Numerical analysis of seismic wave amplifica-		1003
940	Advanced dynamic soil testing — introducing the new Marum dynamic triaxial		tion in Nice (France) and comparisons with experiments. <i>Soil Dyn Earthq Eng</i> 19:347–		1004
941	testing device. In: Mosher DC, Shipp RC, Moscardelli L, Chaytor JD, Baxter CDP, Lee		362. https://doi.org/10.1016/S0267-7261(00)00016-6		1005
942	HJ, Urgeles R (eds) Submarine mass movements and their consequences: 4th		Shepard FP (1954) Nomenclature based on sand-silt-clay ratios. <i>J Sediment Res</i> 24:151–		1006
943	international symposium. Springer, Dordrecht, pp 31–41		158. https://doi.org/10.1306/D4269774-2B26-11D7-8648000102C1865D		1007
944	Labbé M, Donnadiou C, Daubord C, Hébert H (2012) Refined numerical modeling of the		Skempton AW (1954) The pore-pressure coefficients a and B. <i>Géotechnique</i> 4:143–147.		1008
945	1979 tsunami in Nice (French Riviera): comparison with coastal data. <i>J Geophys Res</i>		https://doi.org/10.1680/geot.1954.4.4.143		1009
946	117:1–17. https://doi.org/10.1029/2011JF001964		Stegmann S, Kopf A (2014) How stable is the Nice slope? - an analysis based on strength		1010
947	Larroque C, Delouis B, Godel B, Nocquet J-M (2009) Active deformation at the south-		and cohesion from ring shear experiments. In: Krastel S, Behrmann J-H, Völker D,		1011
948	western Alps–Ligurian basin junction (France–Italy boundary): evidence for recent		Stipp M, Berndt C, Urgeles R, Chaytor J, Huhn K, Strasser M, Harbitz CB (eds)		1012
949	change from compression to extension in the Argentera massif. <i>Tectonophysics</i>		Submarine mass movements and their consequences: 6th international symposium.		1013
950	467:22–34. https://doi.org/10.1016/j.tecto.2008.12.013		Springer, Cham, pp 189–199		1014
951	Larroque C, Lépinay D, Mercier B, Migeon S (2011) Morphotectonic and fault–earthquake		Stegmann S, Kopf A, Apprioual R, Pelleau P (2011) Hydrogeology and its effect		1015
952	relationships along the northern Ligurian margin (western Mediterranean) based on		on slope stability along the coastal aquifer of Nice, France. <i>Mar Geol</i> 280:168–181.		1016
953	high resolution, multibeam bathymetry and multichannel seismic-reflection profiles.		https://doi.org/10.1016/j.margeo.2010.12.009		1017
954	<i>Mar Geophys Res</i> 32:163–179. https://doi.org/10.1007/s11001-010-9108-7		Steiner A, Kopf A, Henry P, Stegmann S, Apprioual R, Pelleau P (2015) Cone penetration		1018
955	Larroque C, Scotti O, Ioualalen M (2012) Reappraisal of the 1887 Ligurian earthquake		testing to assess slope stability in the 1979 Nice landslide area (Ligurian margin, SE		1019
956	(western Mediterranean) from macroseismicity, active tectonics and tsunami model-		France). <i>Mar Geol</i> 369:162–181. https://doi.org/10.1016/j.margeo.2015.08.008		1020
957	ling. <i>Geophys J Int</i> 190:87–104. https://doi.org/10.1111/j.1365-246X.2012.05498.x		Sultan N, Cochonat P, Canals M, Cattaneo A, Dennielou B, Hafidason H, Laberg JS, Long		1021
958	Leynaud D, Mulder T, Hanquiez V, Gonther E, Régert A (2017) Sediment failure types,		D, Mienert J, Trincardi F, Urgeles R, Vorren TO, Wilson C (2004) Triggering mecha-		1022
959	preconditions and triggering factors in the Gulf of Cadiz. <i>Landslides</i> 14:233–248.		nisms of slope instability processes and sediment failures on continental margins: a		1023
960	https://doi.org/10.1007/s10346-015-0674-2		geotechnical approach. <i>Mar Geol</i> 213:291–321. https://doi.org/10.1016/j.margeo.2004.10.011		1024
961	Liu AH, Stewart JP, Abrahamson NA, Moriwaki Y (2001) Equivalent number of uniform		Sultan N, Savoye B, Jouet G, Leynaud D, Cochonat P, Henry P, Stegmann S, Kopf A (2010)		1025
962	stress cycles for soil liquefaction analysis. <i>J Geotech Geoenviron</i> 127:1017–1026.		Investigation of a possible submarine landslide at the Var delta front (Nice continental		1026
963	https://doi.org/10.1061/(ASCE)1090-0241(2001)127:12(1017)		slope, Southeast France). <i>Can Geotech J</i> 47:486–496. https://doi.org/10.1139/T09-105		1027
964	Loizeau J-L, Arbouille D, Santiago S, Vernet J-P (1994) Evaluation of a wide range laser		Thomas Y, Apprioual R (2015) STEP 2015 cruise, L'Europe R/V. doi: https://doi.org/10.17600/15006100		1028
965	diffraction grain size analyser for use with sediments. <i>Sedimentology</i> 41:353–361.		Wang H, Wen R, Ren Y (2017) Simulating ground-motion directivity using stochastic		1029
966	https://doi.org/10.1111/j.1365-3091.1994.tb01410.x		empirical Green's function method. <i>Bull Seismol Soc Am</i> 107:359–371. https://doi.org/10.1785/0120160083		1030
967	Migeon S, Mulder T, Savoye B, Sage F (2006) The Var turbidite system (Ligurian Sea,		Wiemer G, Kopf A (2017) On the role of volcanic ash deposits as preferential submarine		1031
968	northwestern Mediterranean)—morphology, sediment supply, construction of turbid-		slope failure planes. <i>Landslides</i> 14:223–232. https://doi.org/10.1007/s10346-016-0706-6		1032
969	dite levee and sediment waves: implications for hydrocarbon reservoirs. <i>Geo-Mar Lett</i>				1033
970	26:361–371. https://doi.org/10.1007/s00367-006-0047-x				1034
971	Migeon S, Cattaneo A, Hassoun V, Dano A, Casadevant A, Ruellan E (2012) Failure				1035
972	processes and gravity-flow transformation revealed by high-resolution AUV swath				1036
973	bathymetry on the Nice continental slope (Ligurian Sea). In: Yamada Y, Kawamura K,				1037
974	Ikehara K, Ogawa Y, Urgeles R, Mosher D, Chaytor J, Strasser M (eds) Submarine mass				1038
975	movements and their consequences: 5th international symposium. Springer, Dor-				1039
976	drecht, pp 451–461				1040
977	Mulder T, Savoye B, Piper DJW, Syvitski JPM (1998) The Var submarine sedimentary				1041
978	system: understanding Holocene sediment delivery processes and their importance to				1042
979	the geological record. <i>Geol Soc Lond, Spec Publ</i> 129:145–166. https://doi.org/10.1144/GSL.SP.1998.129.01.10				1043
980	Mullis JP, Arulanandan K, Mitchell JK, Chan CK, Seed HB (1977) Effects of sample				1044
981	preparation on sand liquefaction. <i>J Geotech Eng Div</i> 103:91–108				1045
982	Nocquet J-M (2012) Present-day kinematics of the Mediterranean: a comprehensive				1045 Q2
983	overview of GPS results. <i>Tectonophysics</i> 579:220–242. https://doi.org/10.1016/j.tecto.2012.03.037				1046
984	Rehault J-P, Boillot G, Mauffret A (1984) The western Mediterranean basin geological				1047
985	evolution. <i>Mar Geol</i> 55:447–477. https://doi.org/10.1016/0025-3227(84)90081-1				1048
986	Sadrekarami A, Olson SM (2011) Critical state friction angle of sands. <i>Géotechnique</i>				1049
987	61:771–783. https://doi.org/10.1680/geot.9.P.090				1050
988	Sahal A, Lemahieu A (2011) The 1979 Nice airport tsunami: mapping of the flood in				1051
989	Antibes. <i>Nat Hazards</i> 56:833–840. https://doi.org/10.1007/s11069-010-9594-6				1052
990	Salichon J, Kohrs-Sansorny C, Bertrand E, Courboux F (2010) A mw 6.3 earthquake				1053
991	scenario in the city of Nice (Southeast France): ground motion simulations. <i>J Seismol</i>				1054
992	14:523–541. https://doi.org/10.1007/s10950-009-9180-0				1055
993					
994					

A. Roesner (✉) · G. Wiemer · S. Kreiter · S. Wenau · T.-W. Wu · V. Spiess · A. Kopf

MARUM—Center for Marine Environmental Sciences,
University of Bremen,
Bremen, Germany
Email: aroesner@uni-bremen.de

S. Wenau · V. Spiess

Faculty of Geosciences,
University of Bremen,
Bremen, Germany

F. Courboux

Université Côte d'Azur CNRS, IRD, Observatoire de la Côte d'Azur, Géoazur,
Valbonne, France